CHALMERS
UNIVERSITY OF TECHNOLOGY

Sigma-Delta-Over-Fiber With WDM Serial Connection for Distributed MIMO

Citation for the original published paper (version of record):
Olofsson, F., Aabel, L., Eriksson, T. et al (2025). Sigma-Delta-Over-Fiber With WDM Serial Connection for Distributed MIMO. Journal of Lightwave Technology, 43(5).
http://dx.doi.org/10.1109/JLT.2024.3490696

(article starts on next page)

Sigma-Delta-Over-Fiber With WDM Serial Connection for Distributed MIMO

Frida Olofsson, Lise Aabel, Thomas Eriksson, *Member, IEEE,*
Magnus Karlsson, *Fellow, Optica, Fellow, IEEE,* and Christian Fager, *Senior Member, IEEE*

***Abstract*—In this paper, we investigate the first downlink with serially connected remote radio heads (RRHs) using sigma-delta-over-fiber (SDoF) for distributed MIMO (D-MIMO). Coarse wavelength-division multiplexing (CWDM) is used and one wavelength is assigned to each RRH. The serial connection architecture is implemented with passive off-the-shelf components. Specifically, signals are combined into one fiber cable by using an optical multiplexer (MUX) and signals are dropped at each RRH by using optical add-drop multiplexers (OADMS). The architecture implementation is scalable in terms of energy consumption and cost. We measure the sensitivity of SDoF towards the optical interference that occurs when several signals are combined into one fiber, and compare to alike measurements using analog radio-over-fiber (ARoF). We also address the challenge of different time-delays to each RRH, due to the different fiber lengths; we present a method for time-delay compensation, which makes the architecture using RRHs connected in series perform similarly to using RRHs connected in parallel. Finally, our measurements show that the architecture with serially connected RRHs can be used to serve two user equipment (UEs) simultaneously within the same time- and frequency resources, using multi-user MIMO technologies.**

***Index Terms*—Distributed multiple-input-multiple-output (MIMO), sigma-delta-over-fiber (SDoF), optical fronthaul, wavelength-division multiplexing (WDM).**

I. Introduction

THE demand for higher capacity, lower latency and better coverage grows as we move into the 6G era [1]. Distributed MIMO (D-MIMO) is a key technology to reach these targets, providing more uniform coverage, less shadow fading, higher energy efficiency and low spatial correlation between channels [2]. Fig. 1 shows a D-MIMO network, where one central unit (CU) is connected to several remote radio heads (RRHs), in contrast to the centralized cellular MIMO system. To gain the greatest benefit with D-MIMO, the RRHs should transmit coherently [3, Ch. 1], which requires radio frequency (RF) phase synchronization among all RRHs [4]. For a base station in the centralized cellular MIMO system, a common reference clock can be used to assure synchronization, due to the physical proximity of the antennas. But for spatially distributed RRHs, having access to a common clock at each location is not trivial, and even though D-MIMO has been widely investigated in theory [3], hardware implementations are few. The demonstrated implementations with RF phase-synchronized distributed RRHs have used either clock reference distribution over the fronthaul [5] or air [6], or central frequency up-conversion [7]. Central frequency up-conversion is a prominent solution as no synchronization is needed in the RRHs. The cost is that RF-signals instead of baseband signals are transmitted over the fronthaul, increasing the required sample rate in the CU and the fronthaul data rate.

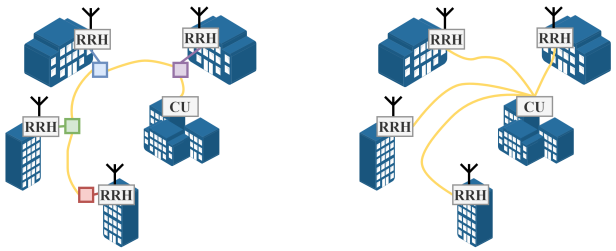

Fig. 1. Distributed MIMO system with (a) serially connected and (b) parallel connected remote radio heads (RRHs) connected to a central unit (CU).

Optical fibers are considered good candidates for connecting the CU to the RRHs, due to their low loss and high bandwidth. Different techniques can be used to modulate the RF-signals onto the optical carrier, associated with different radio-over-fiber technologies. The most promising technologies for D-MIMO systems are analog radio-over-fiber (ARoF) and (bandpass) sigma-delta-over-fiber (SDoF), due to their simple design of RRHs [8]. In ARoF, the RF-signal is directly modulated onto an optical carrier. It has the advantage of high spectral efficiency, but the drawback of being sensitive to non-linearities in the optical components [9]. The feasibility of using ARoF for D-MIMO was demonstrated in [10] and [11], where four phase coherent RRHs were implemented—one connected to the CU with an ARoF link and three with coaxial cables. Measurement results showed an SNR gain of 9.4 dB when transmitting coherently from the four RRH, approaching the theoretical value of 12 dB. Experimental demonstrations of D-MIMO using ARoF technologies were also done in [12], [13] and [14]. In [12] it was shown how D-MIMO can be used

This work has been financed by the Swedish Reseacrh Council under Grant VR-2019-05174.

F. Olofsson, M. Karlsson and C. Fager are with the Department of Microtechnology and Nanoscience, Chalmers University of Technology, 41296 Gothenburg, Sweden (e-mail: frida.olofsson@chalmers.se; magnus.karlsson@chalmers.se; christian.fager@chalmers.se).

L. Aabel is with Ericsson AB, 41756 Gothenburg, Sweden, and also with the Department of Electrical Engineering, Chalmers University of Technology, 41296 Gothenburg, Sweden (e-mail: lise.aabel@ericsson.com).

T. Eriksson is with the Department of Electrical Engineering, Chalmers University of Technology, 41296 Gothenburg, Sweden (e-mail: thomase@chalmers.se).

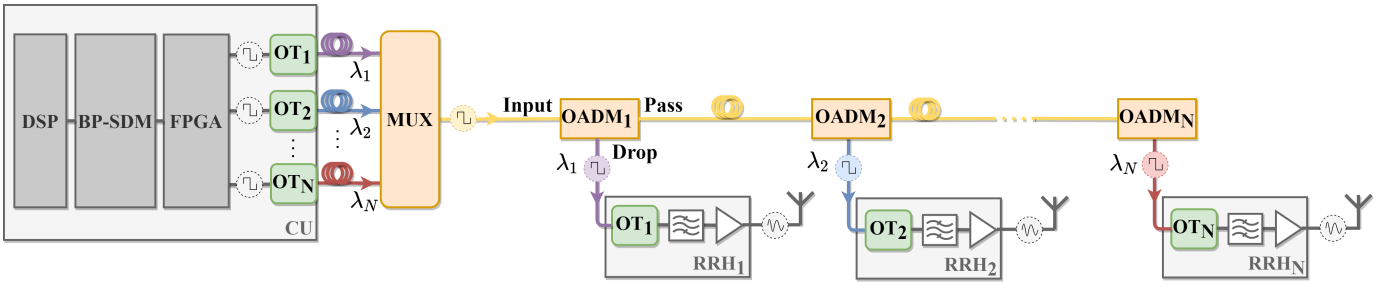

Fig. 2. Schematic of the sigma-delta-over-fiber (SDoF) architecture with N serially connected remote radio heads (RRHs) using wavelength-division multiplexing (WDM). In the central unit (CU) digital signal processing (DSP) and bandpass sigma-delta modulation (BP-SDM) are performed, and the output bitstreams are written to the FPGA that is connected to N transmitting optical transceivers (OTs) of different wavelengths. The optical signals are combined in the optical multiplexer (MUX) and transmitted over fiber. At each RRH one signal is dropped using optical add-drop multiplexers (OADMs) and inserted to the receiving OT. The output electrical signal from the OT is bandpass filtered to recover the original radio frequency signal, amplified with the power amplifier (PA) and transmitted over-the-air (OT) with the patch antenna. The signal characteristics, binary or RF-signal, are marked at the output of the OTs, MUX, OADMs and RRHs.

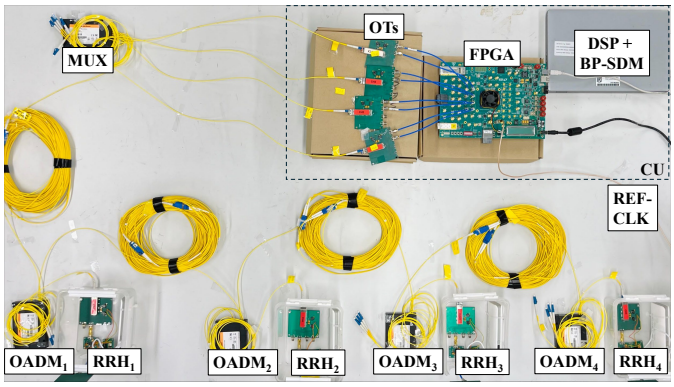

Fig. 3. The experimental configuration with four serially connected remote radio heads (RRHs) including: central unit (CU), digital signal processing (DSP), bandpass sigma-delta modulation (BP-SDM), field-programmable gate array (FPGA), reference clock (REF-CLK), optical transceivers (OTs), optical multiplexer (MUX) and optical add-drop multiplexers (OADMs).60 m optical fiber cable connects the CU to the first OADM as well as each OADM to the following.

to mitigate the effect of blockage, based on antenna selection technologies using carrier frequencies of 28 GHz. The experimental demonstration presented in [13] also used D-MIMO and carrier frequencies of 28 GHz, but instead cooperation among the RRHs to create a stable throughput by overcoming blockage. In [14, Sec. 1] D-MIMO with RRHs that cooperated using partial MMSE precoding was shown, and a more uniform throughput over the demonstration area was achieved. In SDoF, the high-resolution RF-signal is converted to a bitstream at the cost of high oversampling [15, Ch. 1], and transmitted as a binary signal over the fiber [16]. The binary nature of SDoF displays higher robustness towards non-linearities than ARoF [9] and supports the use of low-resolution components. In fact, SDoF allows us to use low-cost optical interconnects developed for data centers, and it becomes feasible to scale up the number of RRHs—as expected in D-MIMO. In [7] and [17] it was demonstrated that SDoF enables coherent downlink transmission from distributed RRHs. In [18], an uplink architecture was demonstrated showing that reciprocity-based time-division duplex D-MIMO with RF phase-synchronized RRHs is enabled by using binary optical transmission, with SDoF in the downlink and dithered 1-bit quantization in the uplink.

Even though it was shown in [7], [17] and [18] that SDoF provides high scalability in terms of electrical hardware as the number of RRHs increases, the solution for the optical connection between CU and RRHs is not scalable. In particular, using one optical fiber to connect each RRH to the CU becomes impractical in a system with a large number of RRHs. In [19], a scalable implementation of the fronthaul in D-MIMO networks was discussed in theory, where the RRHs were serially connected using electrical cables in so called radio-stripes [20]. Serial connection of the RRHs enhance implementation scalability significantly in architectures with a dense distribution of RRHs. Scenarios that require a dense distribution of RRHs are in general also scenarios where D-MIMO has large potential to improve performance compared to centralized MIMO, for example public squares, stadiums, airports, warehouses and factories [21]. Network densification is also a key factor to enable the use of higher carrier frequencies and enhance energy efficiency in wireless networks [22], [23]. Wavelength-division multiplexing (WDM) can be used to implement the serial connection optically. A conceptual discussion of optical serial connection using WDM with ARoF was done in [24], where two distributed antenna units were proposed to transmit coherently to the user equipments (UEs) in one cell. However, the distributed antenna units were not located on the same serial stripe, but at different stripes at the same distance from the CU, hence different time delays in the fibers were not addressed. In [25] an experimental demonstration of four serially connected distributed antenna units using WDM with ARoF was done, but coherent joint transmission was not implemented.

In this paper we investigate the first SDoF architecture with serially connected RRHs and coherent joint transmission—for D-MIMO, see Fig. 1. The downlink signals at the RRH are RF phase-synchronized due to central frequency up-conversion, and serially connected using WDM with one wavelength

assigned to each RRH. We perform over-the-air (OTA) measurements with four serially connected RRHs, serving two UEs within the same time- and frequency resources, using multi-user MIMO technologies. We also evaluate the architecture in terms of interference sensitivity and delay compensation sensitivity. Due to the reciprocity of the optical link we only present investigations of the downlink, but the architecture can be extended to involve also the uplink using the concept presented in [18]. Our results show that, by using delay compensation techniques the same performance can be achieved when connecting the RRHs in series compared to in parallel. This fact makes SDoF with WDM a competitive fronthaul solution in terms of scalability for downlink D-MIMO.

The rest of this paper is structured as follows. In Section II we present the serially connected WDM SDoF architecture. We investigate in Section III impairments introduced by the hardware components and theoretical limitations on the fiber length. In Section IV we evaluate the complete architecture using OTA measurements. The potential of the architecture in D-MIMO is presented in Section V, with multi-user MIMO measurements. In Section VI we discuss the scalability of the proposed solution, and in Section VII we make some concluding remarks.

II. WDM SDoF ARCHITECTURE

A conceptual schematic of the proposed downlink architecture, with N serially connected RRHs, based on WDM and SDoF is presented in Fig. 2. In the CU, one bitstream per RRH is created using sigma-delta modulation and converted from electrical to optical domain using optical transceivers (OTs). The optical outputs from N OTs are combined using an optical multiplexer (MUX) and transmitted over one optical fiber. At each RRH, the corresponding wavelength is dropped using an optical add-drop multiplexer (OADM), and inserted to the receiving port of an OT. The electrical output signal from the OT is bandpass filtered, amplified and transmitted OTA.

The architecture with RRHs connected in series in Fig. 1a can be compared to a parallel architecture in Fig. 1b, where one fiber is used to connect each RRH to the CU. To investigate the proposed architecture, we built the experimental configuration shown in Fig. 3, with four serially connected RRHs. In this section, we describe the communication signal and hardware used in our experimental configuration.

A. Communication Signal

In the CU, QAM symbols are constructed and pulse-shaped with a root-raised-cosine filter using a roll-off of 0.2. The baseband signals are digitally up-converted to single-carrier RF-signals. Two-level bandpass sigma-delta-modulation (BP-SDM) transform the RF-signal to a bitstream [15, Ch. 1]. When quantizing a signal with only two levels a large quantization error occurs, and the original signal is distorted. However, SDM uses high oversampling and noise shaping to make it possible to recover the original signal with small distortion [16]. In the receiver, at the UE, the RF-signal is demodulated by: down-conversion to baseband, down-sampling and matched filtering.

B. Experimental Configuration

Our experimental configuration of the proposed architecture in Fig. 2 is shown in Fig. 3 and consists of the CU, SDoF links and four RRHs. The CU consists of a computer, a field-programmable gate array (FPGA) evaluation board (Transceiver Signal Integrity Development Kit, Stratix V GT Edition) [26] and four OTs (FS, CWDM-SFP10G-10M). Two-level BP-SDM signals are generated using the Delta Sigma toolbox [15, App. B] in MATLAB and written from the computer to the FPGA. An external signal generator is connected to the FPGA and used as reference clock, with frequency of 156.25 MHz. Four OTs are connected to digital 10 GS/s FPGA outputs. The OT transmitter accepts binary voltage inputs and outputs an on-off coded optical signal. We use OTs of four different wavelengths in the coarse WDM (CWDM) spectrum, $\lambda = \{1510, 1530, 1550, 1570\}$ nm.

The OTs are connected to the MUX (FS, 70412) via optical single-mode-fibers (FS, 40191). In the MUX, the four signals of different wavelengths are combined into one single fiber. At each RRH, an OADM (FS, 70425) is used to filter out one of the wavelengths and pass the other ones through. The optical signal of the dropped wavelength is inserted to another OT of the same wavelength, which performs optical to electrical conversion.

In the RRH, the electrical output signal of each OT is filtered with a bandpass filter (Qorvo 885075), to convert the binary SDM signal back to the underlying RF-signal. The bandpass filter has a bandwidth of 100 MHz, from 2.3 to 2.4 GHz. After filtering, the RF-signal is amplified with a power amplifier (PA) of 36 dB gain, to achieve enough power for OTA transmission. The PA (Qorvo TQP9424) has a bandwidth of 100 MHz, from 2.3 to 2.4 GHz. For OTA transmission, an in-house designed patch antenna is connected to the output of the PA. The patch antenna is designed with a gain of 3 dBi, directivity of 6.5 dBi and a half-power beam width of 176°.

III. IMPAIRMENT INVESTIGATIONS

When connecting the RRHs in series instead of in parallel, different impairments may emerge. In this section, we identify and investigate the most dominant impairments through theoretical analysis and extensive wired optical and electrical measurements of important components in the proposed architecture. Throughout this section, single-carrier communication signals with 20 MBd symbol rate and a carrier frequency of 2.35 GHz are used.

A. Sensitivity

Due to the serial connection, the propagation distance between the CU and each RRH is different. The propagation loss in the optical fiber increases with distance, and optical signals of varying power will therefore reach each of the receiving

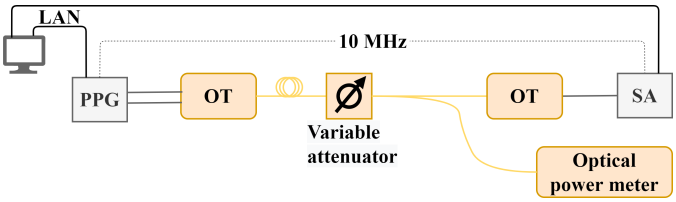

Fig. 4. Setup for measuring the sensitivity of the optical transceiver (OT), including: pulse pattern generator (PPG), transmitting and receiving OT, variable optical attenuator, optical power meter and signal analyzer (SA).

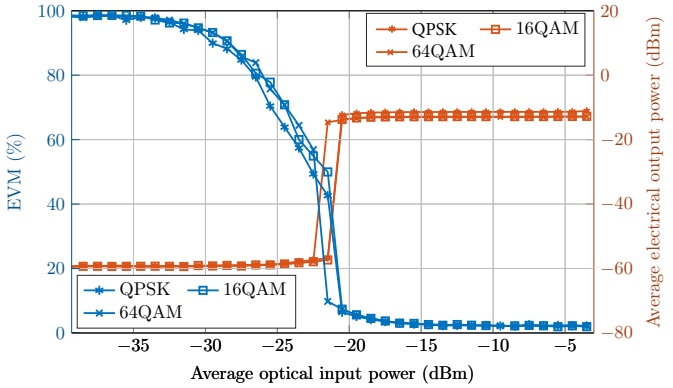

Fig. 5. Error vector magnitude (EVM) and average electrical output power for three different orders of QAM modulation

when sweeping the average optical input power to the receiving optical-transceiver (OT), using the setup in Fig. 4.

OTs in the RRHs. Furthermore, the OADMs introduce losses for both the signals dropped and passed. As a consequence, the optical power in each receiving OT depends on how many OADMs a signal of the corresponding wavelength has passed. We use the setup in Fig. 4 to investigate the effect of the optical input power to the OTs on the EVM and output electrical power, hence the sensitivity. Two OTs are connected through 60 m optical fiber, one is used to transmit and one to receive. We insert a variable optical attenuator and an optical power meter—using a 10 dB coupler—before the receiving OT to control and monitor the received optical power. A pulse pattern generator (PPG, Anritsu, MP1900A) is used to feed an SDM signal to the transmitting OT. Note that the transmitting OT outputs a constant average optical power for all electrical input voltages in a specified range (180-700 mV). Therefore the input voltage level to the OT is fixed at 700 mV for all measurements. The output electrical signal from the receiving OT is sampled with a signal analyzer (SA, Keysight, N9030A). The SA is synchronized to the transmitting PPG through a 10 MHz reference clock.

We sweep the average optical input power to the receiving OT using the variable optical attenuator. In Fig. 5 we present the error vector magnitude (EVM) of the received symbols, and the average electrical output power of the receiving OT, as a function of the average optical input power, for three different orders of QAM modulation. We observe that the average electrical output power remains at −12 dBm when the average optical input power is larger than −21 dBm. We also observe that the EVM is improved past the operational point of −21 dBm average optical input power, and remains constant when the power is larger than −15 dBm. The decrease in EVM for constant average electrical output power is due to increased SNR. A small difference is noted in both EVM and average electrical output power for the measurements using 64QAM modulation compared with QPSK and 16QAM. We conclude from Fig. 5 that the number of RRHs and the length of fiber-optical cables should result in a total loss low enough to ensure that the average optical input power at each of the receiving OTs is larger than −15 dBm.

B. Fiber Dispersion, Loss and Nonlinear Distortion

The maximum number of RRHs and the maximum fiber length to the furthest RRH are limited by fiber dispersion, loss and nonlinear distortion. We analyze theoretically how these factors impact the feasible fiber length. We restrict the analysis to a maximum of 18 RRHs, based on the number of available wavelength channels in the standardized CWDM spectrum [27]. To address various system configurations we consider a maximum total fiber length of 10 km, even though we expect the scenarios presented in the introduction to be implemented with shorter fiber lengths. 10 km is also a typical fronthaul distance in radio access networks.

1) Fiber Dispersion: The time delay between two wavelength components separated with $\Delta\lambda$ induced by fiber group velocity dispersion (GVD) can be estimated using

$$\Delta t_D = D\Delta\lambda L, \tag{1}$$

where D is the dispersion coefficient in the fiber and L is the total fiber length. GVD induces both a time delay between different wavelength components within each CWDM channel and a walk-off between the different CWDM channels. The dispersion coefficient is wavelength dependent, so to estimate an upper limit we use the highest dispersion coefficient value in the CWDM band of $D = 23.7\,\mathrm{ps}\cdot\mathrm{nm}^{-1}\mathrm{km}^{-1}$ at $\lambda = 1625\,\mathrm{nm}$ [28]. Within each CWDM channel the maximum signal bandwidth is limited by the bandpass filter in the RRH to 100 MHz, which converts to a wavelength bandwidth of approximately 0.01 nm. We calculate the maximum time delay to 2.4 ns, which is small compared to the symbol time of a 100 MBd signal. To estimate an upper limit on the largest walk-off we use the maximum value of D and the largest wavelength separation. The wavelength separation is $\Delta\lambda_{\mathrm{CH1,CH18}} = (N-1)\cdot\Delta\lambda_{\mathrm{CWDM}}$ where $\Delta\lambda_{\mathrm{CWDM}} = 20\,\mathrm{nm}$ is the wavelength spacing between each channel. For $N = 18$ and $L = 10\,\mathrm{km}$, the maximum walk-off is 80 ns, which corresponds to the propagation time in 16 m fiber. The walk-off is constant and much smaller the propagation delay in 10 km optical fiber, hence it can also be compensated for with the time-delay compensation discussed in Section IV-B. By choosing wisely the order sequence of which channels to drop at what RRH, the propagation time-delay and the walk-off can, to some extent, compensate each other.

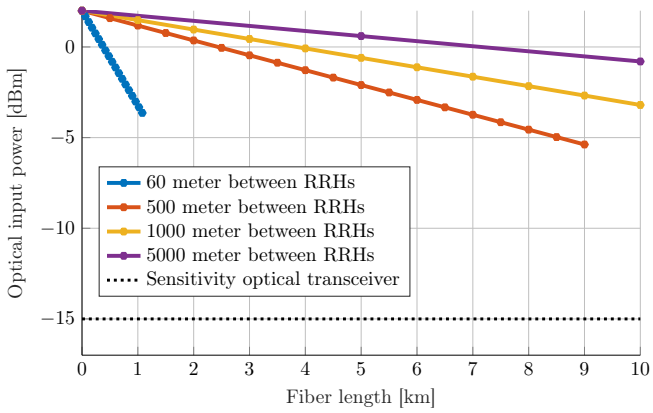

Fig. 6. Optical input power as a function of fiber length based on (3), for four different separation of a maximum of 18 remote radio heads (RRHs). The positions of the RRHs are marked in each curve, resulting in different total fiber lengths for the different RRH separations.

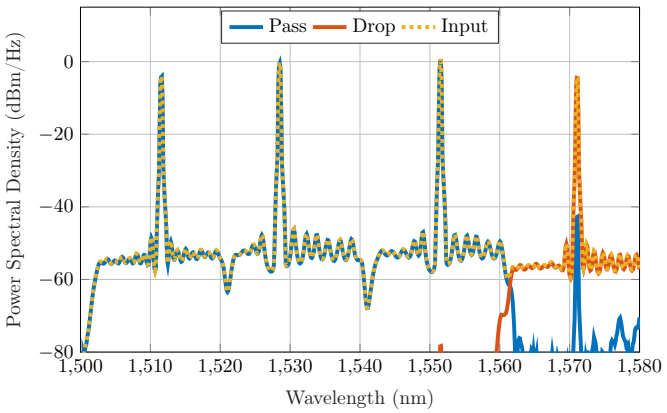

Fig. 7. Optical spectrum at the input, drop and pass port of the 1570 nm optical add-drop multiplexer (OADM). The ports are marked on the first OADM in Fig. 2.

2) Nonlinear Distortion in Fiber: Nonlinear distortion in the fiber results in a phase shift. We estimate the nonlinear phase shift according to

$$\phi_{nl} = \gamma P_{tx} N L_{eff}, \tag{2}$$

where $\gamma = 1.5\,\mathrm{W}^{-1}\mathrm{km}^{-1}$ is the nonlinear coefficient, P_{tx} is the average optical power per channel in W and the effective length is defined as $L_{eff} = (1 - e^{-\alpha L})/\alpha$ where α is the fiber loss coefficient declared in the data sheet as 0.22 dB/km. To avoid nonlinear distortions we require the nonlinear phase shift to be much lower than π rad. We find in the worst case ($N = 18$, $P_{tx} = 2\,\mathrm{dBm}$, $L = 10\,\mathrm{km}$) $\phi_{nl} \approx 0.3\,\mathrm{rad}$ which is an order of magnitude less.

3) Fiber Loss: In Fig. 5 we show that the receiving OTs require a minimum average optical input power of −15 dBm. The minimum optical input power is received at the RRHs furthest from the CU and depends on the optical output power of the transmitting OT in the CU and the total optical loss accumulated by the signal associated with that RRH. The optical output power of the OT is measured as 2 dBm. The total loss consists of losses in the MUX, OADMs and optical fibers. We measure the loss in the MUX and OADMs using an optical power meter. We observe that the loss differs slightly for different wavelengths, both in the MUX and the drop and pass port of the OADMs. The measured average loss per added RRH is approximately 0.3 dB. We estimate the optical input power to the furthest RRH as

$$P_{\text{opt,dBm}} = P_{\text{tx,dBm}} - \alpha_M - \alpha_f L - \alpha_O N, \tag{3}$$

where $P_{\text{tx,dBm}}$ is the output power of the transmitting OT in dBm, α_M is the loss in the multiplexer in dB, α_f is the fiber loss in dB/km and α_O is the average loss in the OADM in dB. We show in Fig. 6 the optical input power as a function of fiber length, for four different fiber lengths between the RRHs and a total of 18 RRHs. All configurations results in a optical input power larger than −15 dBm, but only for a RRH separation of $\sim 550\,\mathrm{m}$ we reach a coverage of 10 km with 18 RRHs. We conclude that our architecture can cover fiber lengths up to 10 km with the 18 CWDM wavelengths without being limited by fiber dispersion, nonlinear phase shift or loss.

C. Optical Filtering

The MUX and OADMs are wavelength-selective components, based on passive optical filters. The MUX combines the output from the four transmitting OTs of different wavelengths into one fiber and the OADMs filter out the relevant wavelength from the fiber at each RRH. We investigate the optical filtering of the OADM by measuring the signal at the input, drop and pass port with an optical spectrum analyzer. The input signal to the OADM includes signals from all four wavelengths OTs, combined using the MUX. The drop port is defined as the one connected to the RRH and the pass port as the one connected to the subsequent OADM. In Fig. 2 we have marked the input, drop and pass ports of the first OADM.

We present in Fig 7 the measured optical spectrum at the input, drop and pass ports of the 1570 nm OADM. We note that after the OADM the majority of the input power in the 1570 nm signal exists at the drop port, with an isolation of 40 dB from the pass port. The suppression of the other three wavelength signals is high, as the power spectral density at the drop port is below −60 dBm/Hz for all wavelengths shorter than approximately 1560 nm.

D. Optical Interference

Optical multiplexing can cause interference, if the signals of different wavelengths are detected by the same photodetector (PD). The OADMs ideally have perfect isolation between the ports, such that only one wavelength is dropped at each RRH. In Fig 7 we present the isolation of the specific 1570 nm OADM used in our configuration, but to specify a fundamental minimum requirement on isolation between the pass and drop port we measure the EVM of the received symbols for different levels of optical interference.

To also explore the robustness of SDoF in the context of interference, we compare the EVM achieved using the

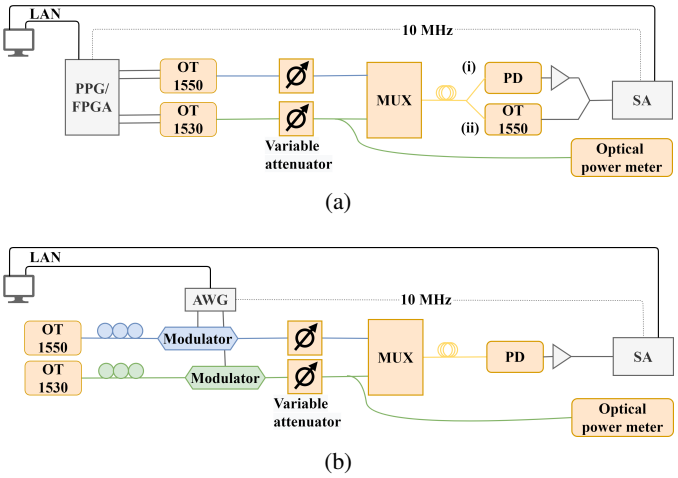

Fig. 8. Measurement setup for investigating interference in (a) analog radio-over-fiber (ARoF) and the (b) sigma-delta-over-fiber (SDoF). (i) and (ii) display the two different receivers used for optical-to-electrical conversion in SDoF. The setups include: pulse pattern generator (PPG), field-programmable gate array (FPGA), arbitrary waveform generator (AWG), optical transceiver (OT), variable attenuator, optical multiplexer (MUX), photodetector (PD), signal-analyzer (SA).

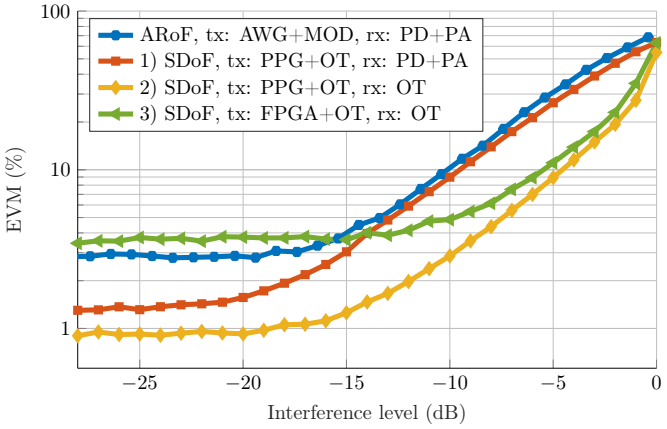

Fig. 9. Error vector magnitude (EVM) versus interference level for the analog radio-over-fiber (ARoF) setup and three hardware variants of the sigma-delta-over-fiber (SDoF) setup presented in Fig. 8.

WDM SDoF setup in Fig. 8a to the EVM achieved using the WDM ARoF setup in Fig. 8b. 16QAM symbols are used throughout this section. In the WDM SDoF setup, binary SDM signals with 10 GS/s are generated in the CU, using either the PPG (Anritsu, MP1900A) or the FPGA, and fed to the OTs. In the WDM ARoF setup, RF signals are instead generated in the CU using the arbitrary waveform generator (AWG, Agilent Technologies, M8190A), and modulated onto the optical carrier that is output from the OTs, using optical intensity modulators (JDS Uniphase, OC-192 10024180). In both setups, the optical signals are combined using the MUX. The isolation level of an OADM is emulated using variable optical attenuators that are placed before the MUX, to control the power of the signal. For the 1530 nm signal the average optical power is also monitored using an optical power meter inserted with a 10 dB coupler. The power of the 1550 nm optical signal is measured and remains constant during the measurement.

In the WDM SDoF setup, two different receivers are used: the 1550 nm OT or a PD (Thorlabs, DET08CFC) with 5 GHz bandwidth followed by a PA (Mini-Circuits, ZHL-42W-SMA). In the WDM ARoF setup, the signal is received using the PD (Thorlabs, DET08CFC) and PA (Mini-Circuits, ZHL-42W-SMA). Note that the OT can not be used as receiver in the WDM ARoF setup, because it is designed to operate non-linearly to receive binary signals. The output electrical signal from the receiving OT or PD + PA is sampled with a SA (Keysight, N9030A). The SA is synchronized to the transmitting PPG, AWG and FPGA through a 10 MHz reference clock.

1) Comparison Between SDoF and ARoF: Firstly, we investigate how the EVM of the received symbols, transmitted at the 1550 nm signal is affected when the optical power of the interfering 1530 nm signal increases, which indicates the isolation requirement between the OADM pass and drop ports. The average optical power is constant −7.5 dBm for the 1550 nm signal and swept from −35.5 dBm to −7.5 dBm for the 1530 nm signal.

In Fig. 9 we present measured EVM of the received symbols as a function of the interference level: $P_{opt,1530\text{nm}}/P_{opt,1550\text{nm}}$. In the ARoF setup, the AWG and modulator are used as transmitter, and PD + PA as receiver. The SDoF setup is measured in three different hardware variants:

1) transmitter (tx): PPG + OT, receiver (rx): PD + PA,
2) tx: PPG + OT, rx: OT,
3) tx: FPGA + OT, rx: OT.

We hereon refer to these variants as SDoF hardware variant #1, #2 and #3, respectively. At low levels of interference, EVM remains constant as the interference increases for all four configurations. This implies that the communication performance in that region is not limited by optical interference, and different sources limit the EVM performance for the different setups and hardware variants. The SDoF hardware variants #1 and #2 are limited by SNR in the receiving PD + PA or OT, which results in the EVM of 1.3 % and 0.9 %, respectively. The SDoF hardware variant #3 is limited by additional noise in the FPGA, and the lowest value of the EVM is 3.5 %. The additional FPGA noise was further studied in both [7] and [18]. In [7] it was shown through measurements that the FPGA noise level is higher than both the noise from the optical interface and the quantization noise for symbol rates up to 35 MBd. In [18] the source of the additional noise was investigated by measuring the output pulses from both the PPG and the FPGA in time domain, showing a larger amplitude reduction and phase instability in the output pulses from the FPGA. The WDM ARoF setup is also limited by SNR in the receiving PD + PA, but due to the necessity of operating the intensity modulators at low power to avoid distortion, we get a minimum EVM of 3.2 %.

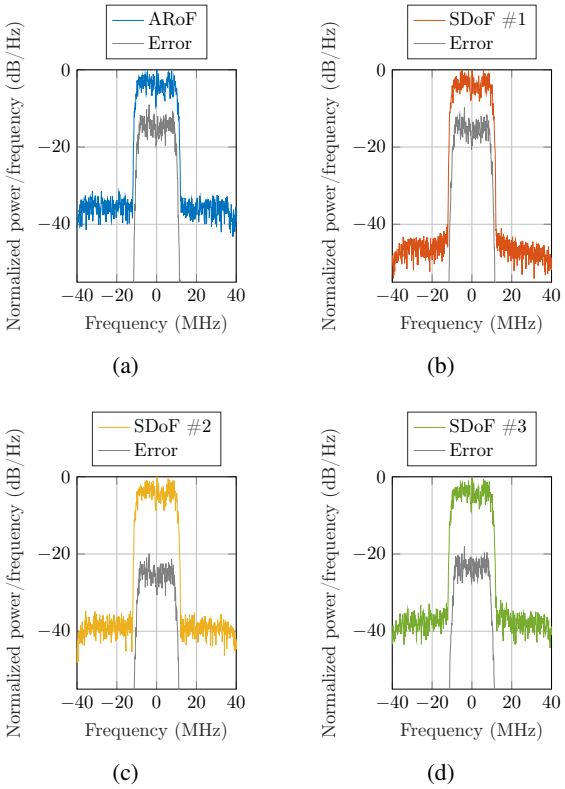

Fig. 10. Normalized spectrum of the received baseband signals and the error for (a) ARoF setup, (b) SDoF hardware variant #1, (c) SDoF hardware variant #2 and (d) SDoF hardware variant #3. The error is the difference between the transmitted and received constellation symbols.

As we increase the level of interference, it starts to limit the communication performance, and the EVM increases. We highlight that in this region the EVM performance for all setups and hardware variants is limited by the interference level and not the sources discussed in the previous paragraph. As a consequence we can make comparisons and investigate if there is a difference in how much optical interference the different setups and hardware variants tolerate. The WDM ARoF setup and SDoF hardware variant #1 experience a similar effect on the EVM, indicating that when receiving with the same hardware (PD + PA) there is no difference between transmitting the RF-signal or the SDM RF-signal. We note that for the SDoF hardware variant #2 a higher level of interference is tolerated before the measured EVM begins to increase, compared with the SDoF hardware variant #1, indicating a higher resilience toward optical interference. Despite the increased noise floor introduced by the FPGA, the EVM measured using the SDoF hardware variant #3 is similar to the EVM measured using the SDoF hardware variant #2 in the large interference regime. Since the SDoF hardware variant #2 and #3 uses the same hardware for receiving the optical signal, it indicates that the OT has preferable properties in the presence of interference compared with the PD + PA. The OT properties are discussed further in Section III-D2.

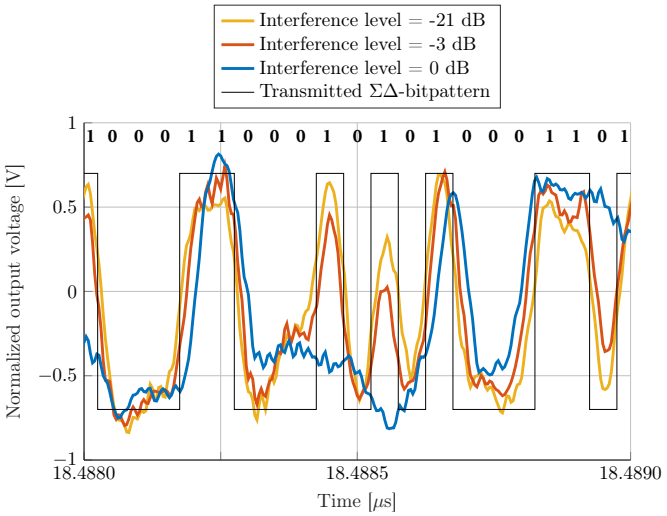

Fig. 11. Output voltage of the receiving optical-transceiver (OT) for three levels of interference and the transmitted sigma-delta modulated (SDM) bit pattern. The symbol rate is 20 MBd and the signals are sampled with 128 GS/s.

In Fig. 10a-d we present the spectrum of the received signal together with the spectrum of the error for an interference level of −5 dB. The error spectrum is the difference between the transmitted and received constellation symbols, presented in frequency domain. The in-band power of the error spectrum is higher for the measurements using the WDM ARoF setup and SDoF hardware variant #1 than for the measurements using SDoF hardware variant #2 and #3, which indicates that a higher power of the interfering signal remains after optical-to-electrical conversion and contributes to the higher EVM.

We conclude that the binary nature of SDM does not itself make SDoF more resilient to optical interference than ARoF, but it facilitates the use of receivers (the OTs) that allows for higher levels of interference. As a consequence also OADMs with lower isolation could be used in an WDM SDoF architecture, compared with an ARoF architecture.

2) Interference Mitigation in the OT: To explain why the OT is more resilient towards optical interference, we investigate the shape of the electrical output pulses for three different levels of interference. We sample the OT electrical output signal with a 128 GS/s, 33 GHz bandwidth oscilloscope (Keysight, UXR0334A). To isolate the effect on the pulse shape from the OT we use the PPG as transmitter and not the FPGA, since it outputs more phase- and amplitude stable pulses [18]. In Fig. 11 we present the measured time-domain-signal, for three levels of interference $\{-21, -3, 0\}$ dB. The perfect square pulse is the transmitted sigma-delta bit pattern. For clarity, also the actual bits (0s and 1s) are visualized.

We observe that—regardless of the interfering power level—the output voltage of the OT is a low pass-filtered version of a square pulse, which is expected due to a limited rise-time in the receiving OT of 30 ps. For the two lowest levels of interference (−21 dB and −3 dB) the pulses correspond to the same bits that were transmitted, even though voltages

TABLE I
ERROR VECTOR MAGNITUDE (EVM) AND SIGMA-DELTA BIT ERROR RATE (BER) OF THE SIGMA-DELTA BITS FOR THREE LEVELS OF OPTICAL INTERFERENCE

Interference level	EVM	Sigma-delta BER
−21 dB	1.0 %	0.002
−3 dB	15.9 %	0.031
0 dB	56.2 %	0.191

close to the threshold of 0 V are observed for the signal with −3 dB interference. For the highest level of interference (0 dB) the pulse shape does not correspond to the transmitted bit at several time instances. The fact that the shape of the pulses is sustained both for the −21 dB and −3 dB level of interference, is attributed to the already mentioned nonlinear operations of the OT. Rather than outputting an electrical pulse that relates linearly to the input optical pulse it works as a comparator, that outputs a one or a zero depending on if the optical input power is above or below a threshold value.

To evaluate how well the OT restores the transmitted bits when affected by optical interference, we evaluate the number of erroneously detected bits in the raw SDM bitstream. We downsample the 128 GS/s time-domain signals to the sample rate of the SDM bit pattern (10 GS/s), and evaluate for each instance if it is a bit 0 or 1 (value above or below 0 V) to compare to the transmitted bits. In Table I we present the sigma-delta BER and the EVM of the received symbols for the three different interference levels. The OT appears to restore most bits, and even for an interference level of −3 dB, only 3 % of the bits are detected erroneously.

IV. OVER-THE-AIR INVESTIGATIONS

Having investigated the performance of the separate components, we in this section study the complete architecture with serially connected RRHs presented in Fig. 2, using OTA measurements and simulations. We use four RRHs, the FPGA as signal source and the OTs for transmitting and receiving the optical signals, as shown in Fig. 3. 60 m optical fiber cable connects the CU to the first OADM as well as each OADM to the following, resulting in a total fiber length of 240 m to the furthest OADM and corresponding RRH. Throughout this section, single-carrier RF-signals with 16-QAM modulation and a carrier frequency of 2.35 GHz are used. The RF-signals are SDM using a sample rate of 10 GS/s. Note that the propagation time from the CU to each RRH is different due to the difference in fiber length, in contrast to an architecture with equal fiber lengths. As a solution, we present an OTA time delay compensation method and evaluate its performance.

A. Channel Estimation and Precoding

In a MIMO system, knowledge about the channel is necessary to implement beamforming. Beamforming is achieved by precoding the transmitted signals, based on the estimated channel, so they arrive phase-aligned at the UEs. In this section, we explain how we perform channel estimation and precoding under the assumption that proper time delay compensation has been performed.

The received signal $\mathbf{y}$ is modelled as

$$\mathbf{y} = \mathbf{H}\mathbf{x} + \mathbf{w}, \tag{4}$$

where $\mathbf{H}$ is the channel matrix, $\mathbf{x}$ is the transmitted signal and $\mathbf{w}$ is additive noise. The channel matrix is estimated using known time-orthogonal downlink pilots. The pilot sequences are transmitted from the four RRHs OTA, and received at each UE position. The received pilot symbols are, in our configuration, sent back to the CU over LAN connection. A least-square estimate of the channel matrix, $\hat{\mathbf{H}}$, is created, using the transmitted and received pilots [29, Ch. 8]. Based on the estimated channel, the signals from the RRHs are precoded. Different precoder matrices can be used. Throughout this section, we construct the precoding matrix $\mathbf{P}$, with the phase of the conjugate of the channel estimations coefficients and the amplitude of the precoding coefficients equal to one as

$$P_{ij} = \frac{\hat{H}^*_{ji}}{|\hat{H}^*_{ji}|}. \tag{5}$$

Note that this precoder maximizes the transmitted power from all RRHs.

B. Time Delay Compensation

Serial connection of the RRHs introduce time delays between the consecutive RRHs, which must be compensated for. We showed in [30] that delay compensation is required to successfully demonstrate coherent joint transmission in the downlink. We measure the relative time-delays between signals from the four RRHs, by transmitting known time-orthogonal sequences. The RRHs are separated by 30 cm, and placed 1.5 m from a SA (Keysight, N9030A) with a patch antenna connected, serving as the UE. The SA is synchronized to the transmitting FPGA with a 10 MHz reference clock. A fixed symbol rate of 20 MBd is used. We calculate the cross-correlation between the transmitted and received baseband signals and estimate the time delay difference. The time delay compensation is performed by delaying the signals in the reverse order at the CU, which ensures that they align time-synchronized at the RRH output ports. By implementing both delay estimation and compensation in frequency domain, sub-sample resolution in time domain is achieved.

In Fig 12a-c we present histograms of the measured relative delays for 70 consecutive measurements. The time delays are presented for RRH_1, RRH_2 and RRH_3 relative to the delay of RRH_4, hence corresponds to the signal propagating through an additional (a) 90 m optical fiber and three OADMs, (b) 60 m optical fiber and two OADMs and (c) 30 m optical fiber and one OADM. We note that the measured relative delays vary less than 1 ns. To investigate if this accuracy is sufficient, we perform measurements with the precoding described in Section IV-A and sweep the delay compensation for two of the RRHs—one at a time. In Fig. 13 we present measured

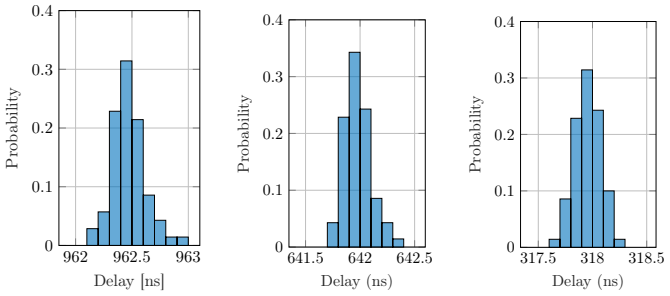

Fig. 12. Histogram of 70 measurements of relative time delay between the fourth remote-radio-head (RRH) and (a) RRH_1, (b) RRH_2, (c) RRH_3. The respective time delays corresponds to the signal propagating through an additional (a) 90 m optical fiber and three OADMs, (b) 60 m optical fiber and two OADMs and (c) 30 m optical fiber and one OADM.

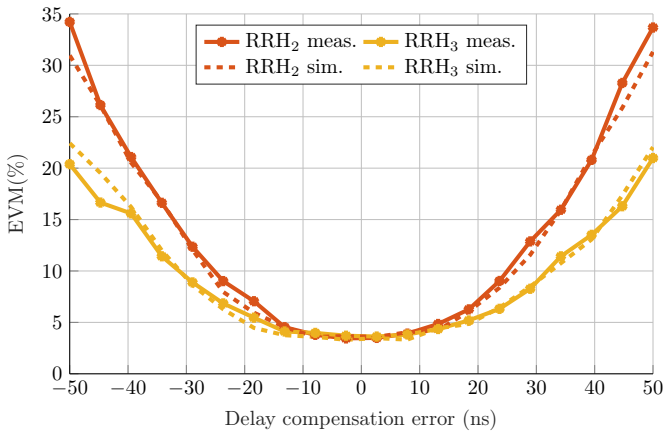

Fig. 13. Error vector magnitude (EVM) of the received symbols when applying inaccurate delay compensation for one remote-radio-head (RRH), while the other three are compensated correctly. Measurements and simulations are presented for when RRH_2 and RRH_3 are compensated erroneously, one at a time. The symbol rate is 20 MBd, giving a symbol time of 50 ns.

EVM of the received symbols as a function of the delay compensation error. We observe that the EVM increases as we make an inaccurate compensation, and for differences close to the symbol-time (50 ns) the EVM has increased more than 15 percentage points for RRH_3 and 30 percentage points for RRH_2 compared to using accurate delay compensation. A difference between RRH_2 and RRH_3 is also seen; the measured EVM is more sensitive to delay compensation error in RRH_2. In these measurements, the estimated $|\hat{H}_{12}| > |\hat{H}_{13}|$, so the effect gets more severe for the RRH associated with the largest channel gain. We simulate the system by replacing $\mathbf{H}$ in (4) with the measured estimated channel matrix, $\hat{\mathbf{H}}$. The simulation results match the measurement results for both RRH_2 and RRH_3, when making inaccurate compensation, see Fig. 13. We thereby confirm that the penalty of delay estimation error scales with the channel gain. By comparing the time scale in Fig. 13 with the variations in the delay

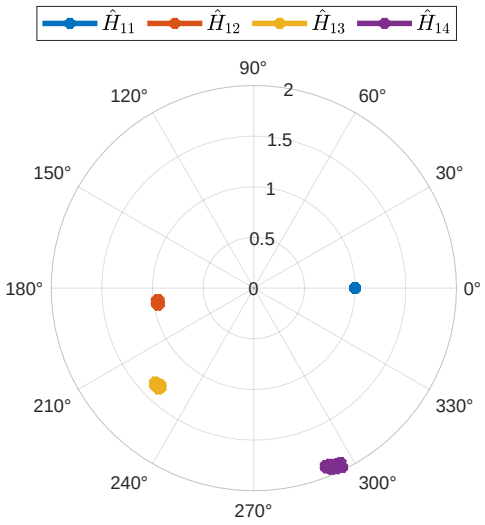

Fig. 14. Estimated channel coefficients for 70 consecutive measurements and one user equipment (UE). The symbol rate is 20 MBd.

measurements of less than 1 ns, we conclude that the delay compensation accuracy is sufficient.

C. Phase Stability

To evaluate the phase synchronization of the transmitted signals from the RRHs, we present in Fig. 14 the estimated channel matrix coefficients for 70 consecutive measurements, using the serially connected RRHs and accurate delay compensation. The symbol rate is 20 MBd. We confirm from Fig. 14 that both the magnitude and phase of the channel estimates are stable over time. The channel estimate coefficient $\hat{H}_{14}$ displays the largest phase drift, with a standard deviation of 0.9 degrees, which we consider to be small [4].

D. Coherent Joint Transmission

We validate the effectiveness of coherent joint transmission by comparing the average received in-band power when transmitting from four RRHs coherently to when transmitting from a single RRH. Theoretically the received power increases with 12 dB when transmitting coherently from four identical transmitters compared with only one transmitter, as the received voltage is four times higher. We measure −14.9 dBm received power at the UE with a single RRH. With four serially connected RRHs transmitting coherently we measure a received power at the UE of −2.1 dBm. Note that we observe a gain of slightly more than 12 dB when transmitting with four RRHs coherently, compared with one RRH. The reason is that even though the signals are precoded with the same amplitude coefficient for maximum transmitted power, we observe variations in the received power from the different RRHs. The variations in received power results from differences in the positions of the RRHs in relation to the UE as well as small variations in the output power of the different RRHs.

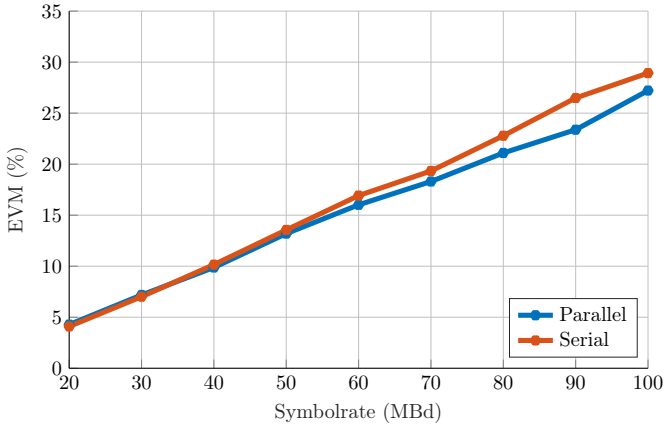

Fig. 15. Error vector magnitude (EVM) of the received symbols as a function of symbol rate for over-the-air (OTA) measurements using the sigma-delta-over-fiber (SDoF) architecture with four remote radio heads (RRHs) connected in serial and parallel.

E. Comparison Between Serial and Parallel

Through OTA measurements we investigate if the serially connected system with delay compensation, Fig.1a, can achieve the same performance in terms of EVM of the received symbols as a system with parallel connection and equal fiber lengths to each RRH, Fig.1b. Here we investigate the EVM for symbol rates in the range of 20 to 100 MBd, using both setups. In the setup connected in parallel, 60 m fiber is used to connect each RRH to the output of the transmitting OT at the CU. An oscilloscope (Rohde&Schwarz RTO1044) with a patch antenna connected serves as UE receiver. The oscilloscope is synchronized to the transmitting FPGA with a 10 MHz reference clock.

In Fig. 15 we present the EVM of the received symbols as a function of the symbol rate. We observe that the measured EVM using the two setups behaves similarly versus symbol rate. In conclusion, connecting RRHs in serial does not introduce any significant penalty on the measured EVM, as long as delay compensation is performed.

V. Distributed Multi-User MIMO

In this section, we use the serially connected SDoF architecture presented in Fig. 2 to perform multi-user D-MIMO measurements. We show that the architecture can simultaneously serve two UEs within the same time- and frequency resources. Throughout this section, single-carrier passband signals with 20 MBd symbol rate, 16-QAM modulation and a carrier frequency of 2.35 GHz are used. The RF-signals are Sigma-Delta-modulated using a sample rate of 10 GS/s.

A. Zero-Forcing Precoder

In a multi-user scenario, we want to use precoding to minimize inter-user-interference. We use the zero-forcing (ZF) precoder to create nulls at the positions of other UEs. The ZF precoder is constructed by inverting the estimate of the channel matrix, $\hat{\mathbf{H}}$, using the Moore Penrose pseudo-inverse, according to [31, Ch. 20]:

$$\mathbf{P}_{\text{ZF}} = \hat{\mathbf{H}}^{\text{H}}(\hat{\mathbf{H}}\hat{\mathbf{H}}^{\text{H}})^{-1}. \tag{6}$$

The received signal for U UEs and T number of RRHs is constructed as

$$\mathbf{y} = \mathbf{H}\mathbf{P}_{\text{ZF}}\tilde{\mathbf{x}} + \mathbf{w}, \tag{7}$$

where $\mathbf{y}$ has dimensions Ux1 and each row corresponds to the received signal at each UE. $\mathbf{H}$ is of dimension UxT. The rows of $\tilde{\mathbf{x}}$ with dimension Ux1 hold the signals to each UE. $\tilde{\mathbf{x}}$ is multiplied with the precoding matrix $\mathbf{P}_{\text{ZF}}$ of dimension TxU to mapp it to a matrix with dimension Tx1, corresponding to the number of antennas. $\tilde{\mathbf{x}}$ relates to $\mathbf{x}$ in (4) as $\mathbf{x} = \mathbf{P}_{\text{ZF}}\tilde{\mathbf{x}}$.

B. Measurements

Here we present measurement results when serving 2 UEs simultaneously using the the ZF precoder. As UE receivers we use two patch antennas connected to two different ports of an oscilloscope (Rohde&Schwarz RTO1044) through one meter long coaxial cables. The oscilloscope is synchronized to the transmitting FPGA with a 10 MHz reference clock. The UE antennas are separated by 1.5 m and placed 2 m from the RRHs, at approximately the same height.

Fig. 16a and 16b show constellation diagrams of the received symbols at UE_1 and UE_2. An equalizer with two taps is applied to the received symbols after demodulation to compensate for inter-symbol interference. An EVM of 10.4 % is achieved at UE_1 and 6.2 % at UE_2. To evaluate what limits the EVM performance, we present the error spectrum and the received signal spectrum in Fig. 16c and 16d, for both UEs. We observe that a certain level of interference occurs, since the power of the error spectrum is higher than the noise floor. Hence, interference limits the EVM performance, rather than thermal noise. The interference can originate from: channel estimation error, leakage between channels in the FPGA, or electromagnetic coupling between the RF circuit boards at the CU or the RRHs. Interference mitigation is an interesting topic for future research. Nevertheless, the EVM at both UEs satisfies the long-term evolution (LTE) and new radio (NR) standards for 16-QAM modulation of 12.5 % [32], and we consider these levels satisfactory.

VI. Discussion

The main reason for introducing the serially connected SDoF architecture is to increase the scalability of D-MIMO. In this section, we discuss the scalability of the proposed architecture, in terms of carrier frequency, bandwidth, the number of RRHs, power consumption and the time delays. Our aim is to highlight that our results are not limited to the experimental configuration presented in Fig. 3. The scalability of the electrical hardware was discussed in [18], we focus therefore on the optical WDM serial connection.

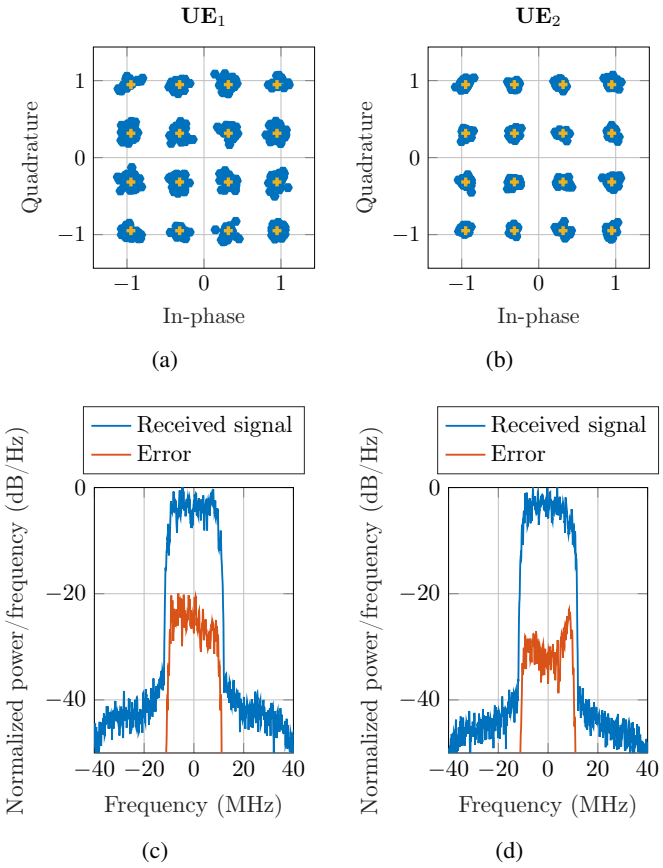

Fig. 16. Constellation diagrams of the received symbols using zero-forcing (ZF) precoding at two user equipments (UEs), (a) UE_1, EVM = 10.4 % and (b) UE_2, EVM = 6.2 %. An equalizer with two taps is applied to the received symbols after demodulation to compensate for inter-symbol interference. The normalized power spectral density of the received signal after down-conversion to baseband as well as the error are presented for (c) UE_1 and (d) UE_2. The error is an up-sampled frequency domain representation of the difference between the transmitted and received symbols.

1) Carrier Frequency and Bandwidth: It was shown in [33] that for SDoF with RRHs connected in parallel, the carrier frequency and bandwidth are limited by the sample rate in the CU and the bandwidths of the electrical components in the RRH. New limitations introduced by the serial connection are the bandwidths of the OADMs and MUX. The OADMs and MUX are passive analog components with bandwidths of approximately 800 GHz (6 nm), hence much larger than the majority of available off-the-shelf electrical components. This means that implementing the serial connection does not put higher requirements on the carrier frequency or bandwidth than in the architecture with the RRHs connected in parallel.

2) Number of Serially Connected RRHs: The standardized CWDM spectrum consists of 18 wavelengths, which limits the number of RRHs per branch. The possibility of connecting more RRHs than 18 could be explored by using dense WDM, which has a narrower wavelength spacing, hence more available wavelengths. Also customized wavelength multiplexing configurations with narrower wavelength spacing could be considered, but at a higher cost. However, a narrower wavelength spacing could also introduce challenges with interference, since the isolation in the optical filter might change. For an increasing number of channels in the fiber it must also be considered that the nonlinear phase shift will increase, which could impose an upper limit on the number of RRHs.

3) Power Consumption: The total optical loss is larger in an architecture with serially connected RRHs compared with an architecture with parallel connected RRHs, due to additional losses in MUX and OADMs. Consequently longer fiber cables can be used in an architecture with the RRHs connected in parallel before the received optical power is too low. The total fiber length that can be covered before the input optical power is lower than the minimum value of −15 dBm is 77 km for a parallel architecture and 52 km for a serial architecture with 18 RRHs, based on (3). The SDoF architecture is relatively resilient to loss in the optical domain, because the SNR at the electrical output of the OT is not linearly dependent on the received optical input power as shown in Fig. 5.. As a result the input power does not need to be increased to compensate for losses in OADMs and MUX, and the power efficiency can be similar to an architecture with RRHs connected in parallel. Nevertheless, the feasible fiber length will be smaller in an architecture with RRHs connected in series than in and architecture with RRHs connected in parallel.

4) Time-Delay: All D-MIMO systems must consider different propagation delays from the CU to the UEs. Propagation delays in the wireless channel can to some extent be managed by the orthogonal frequency-division multiplexing (OFDM) cyclic prefix [34]. Therefore, it would be interesting to operate the proposed architecture using OFDM.

In an implementation with longer optical fiber cables between each serially connected RRH the difference in propagation delays in the fiber will dominate over propagation delays in the air. This may result in increasing access delay and complex time synchronization, limiting the maximum fiber length and making parallel architectures more beneficial. However, for scenarios with a dense distribution of RRHs, such as networks in factories or stadiums, shorter fibers between each RRH are likely. For the maximum total fiber length of 10 km, the propagation time in the fiber to the furthest RRH is 50 μs, which can be compared to the targeted latency of 1 ms in 5G NR [35, Ch. 2]. Further investigations are required to specify the trade-off between access delay, system complexity, and scalability.

VII. Conclusion

We have presented a scalable D-MIMO architecture, based on SDoF and serially connected RRHs. Centralized digital frequency up-conversion assures RF-phase synchronization between the RRHs, making it possible to perform coherent joint transmission to serve several UEs with the same time- and frequency resources, through spatial multiplexing. With measurements, we show that the proposed architecture can perform similarly to an architecture with the RRHs connected

in parallel and fibers of equal length, by using time delay compensation in the CU.

The architecture can support up to 18 serially connected RRHs, using standardized CWDM. More RRHs could potentially be added by using dense WDM technology, which is an interesting future research topic. Future work also includes extending the architecture to involve the uplink proposed in [18]. We believe that the demonstrated architecture provides a scalable, flexible and cost-efficient solution for the deployment of future communication systems.

REFERENCES

[1] G. Wikström *et al.*, "6G – Connecting a cyber-physical world," Ericsson, Stockholm, Sweden, Ericsson white paper, 2022. [Online]. Available: https://www.ericsson.com/en/reports-and-papers/white-papers/a-research-outlook-towards-6g.

[2] S. Zhou, M. Zhao, X. Xu, J. Wang, and Y. Yao, "Distributed wireless communication system: A new architecture for future public wireless access," *IEEE Commun. Mag.*, vol. 41, no. 3, pp. 108–113, Mar. 2003.

[3] Ö. T. Demir, E. Björnson, and L. Sanguinetti, *Foundations of User- Centric Cell-Free Massive MIMO*. Boston, MA, USA, 2021.

[4] E. G. Larsson, "Massive Synchrony in Distributed Antenna Systems," *IEEE Trans. on Signal Process.*, vol. 72, pp. 855–866, Jan. 2024.

[5] H. Bao, F. Ponzini, and C. Fager, "Wideband mm-wave 6×2 distributed MIMO transmitter using sigma-delta-over-fiber," *J. of Lightw. Technol.*, vol. 42, no. 9, pp. 3107–3117, Jan. 2024.

[6] O. Simeone, U. Spagnolini, Y. Bar-Ness, and S. H. Strogatz, "Distributed synchronization in wireless networks," *IEEE Signal Process. Mag.*, vol. 25, no. 5, pp. 81–97, Sep. 2008.

[7] I. C. Sezgin *et al.*, "A low-complexity distributed-MIMO testbed based on high-speed sigma–delta-over-fiber," *IEEE Trans. Microw. Theory Techn.*, vol. 67, no. 7, pp. 2861–2872, Mar. 2019.

[8] L. Breyne, G. Torfs, X. Yin, P. Demeester, and J. Bauwelinck, "Comparison Between Analog Radio-Over-Fiber and Sigma Delta Modulated Radio-Over-Fiber," *IEEE Photon. Technol. Lett.*, vol. 29, no. 21, pp. 1808–1811, Sep. 2017.

[9] F. Olofsson, L. Aabel, M. Karlsson, and C. Fager, "Comparison of Transmitter Nonlinearity Impairments in externally modulated Sigma-Delta-over Fiber vs Analog Radio-over-Fiber links," in *Opt. Fiber Commun. Conf. Exhibit.*, Mar. 2022, pp. 6–9.

[10] R. Puerta *et al.*, "Approaching Theoretical Performance of 6G Distributed MIMO with Optical Analog Fronthaul," in *Conf. on Lasers and Electro-Opt.*, May 2024.

[11] R. Puerta *et al.*, "Analog mobile fronthaul for 6G and beyond," *J. of Lightw. Technol.*, Jul. 2024, Early Access.

[12] NTT DOCOMO. "World's first successful demonstration of distributed mimo that continues wireless connections in the 28 ghz band by eliminating shielding issues." (2022), [Online]. Available: https://group.ntt/en/newsrelease/2022/10/31/221031a.htmll.

[13] KDDI Research Inc. "World first successful demonstration of wireless network deployment methodology for beyond 5G." (2021), [Online]. Available: https://www.kddi-research.jp/english/newsrelease/2021/100701.html.

[14] KDDI Research Inc. "Beyond 5G white paper supplementary volume "cell-free/distributed MIMO"." (2024), [Online]. Available: https://b5g.jp/w/wp-content/uploads/2024/03/Beyond-5G-White-Paper-Supplementary-Volume-Cell-Free-DistributedMIMO.pdf.

[15] S. Pavan, R. Schreier, and G. C. Temes, *Understanding Delta-Sigma Data Converters*, 2nd ed. Hoboken, NJ, USA: John Wiley & Sons, 2017.

[16] L. M. Pessoa, J. S. Tavares, D. Coelho, and H. M. Salgado, "Experimental evaluation of a digitized fiber-wireless system employing sigma delta modulation," *Opt. Express*, vol. 22, no. 14, pp. 17 508–23, Jul. 2014.

[17] C. Y. Wu *et al.*, "Distributed Multi-User MIMO Transmission Using Real-Time Sigma-Delta-Over-Fiber for Next Generation Fronthaul Interface," *J. of Lightw. Technol.*, vol. 38, no. 4, pp. 705–713, Oct. 2020.

[18] L. Aabel, S. Jacobsson, M. Coldrey, F. Olofsson, G. Durisi, and C. Fager, "A TDD distributed MIMO testbed using a 1-bit radio-over-fiber fronthaul architecture," *IEEE Trans. Microw. Theory Techn.*, Apr. 2024, Early Access.

[19] G. Interdonato, E. Björnson, H. Quoc Ngo, P. Frenger, and E. G. Larsson, "Ubiquitous cell-free Massive MIMO communications," *Eurasip J. on Wireless Commun.s and Netw.*, vol. 197, no. 1, pp. 1–13, Aug. 2019.

[20] Ericsson, *Radio stripes: Re-thinking mobile networks*, Ericsson, Stockholm, Sweden, 2019. [Online]. Available: https://www.ericsson.com/en/blog/2019/2/radio-stripes.

[21] O. Haliloglu *et al.*, "Distributed-MIMO Systems for 6G," in *Joint European Conf. on Netw. and Commun. and 6G Summit*, Jun. 2023, pp. 156–161.

[22] H. Q. Ngo, G. Interdonato, E. G. Larsson, G. Caire, and J. G. Andrews, "Ultradense cell-free massive mimo for 6G: Technical overview and open questions," *Proc. of the IEEE*, pp. 1–27, 2024.

[23] E. Björnson, L. Sanguinetti, and M. Kountouris, "Deploying dense networks for maximal energy efficiency: Small cells meet massive MIMO," *IEEE J. on Sel. Areas in Commun.*, vol. 34, no. 4, pp. 832–847, Mar. 2016.

[24] K. Tsukamoto *et al.*, "Convergence of WDM access and ubiquitous antenna architecture for broadband wireless services," *Piers Online*, vol. 1, pp. 773–777, Jan. 2010.

[25] E.-S. Kim, M. Sung, J. H. Lee, J. K. Lee, S.-H. Cho, and J. Kim, "Coverage extension of indoor 5G network

using RoF-based distributed antenna system," *IEEE Access*, vol. 8, pp. 194 992–194 999, Oct. 2020.

[26] Altera Corporation, *Transceiver signal integrity development kit, Stratix V GT edition reference manual*, San Jose, CA, USA, Jan. 2016.

[27] ITU, *G.694.2 : Spectral grids for WDM applications: Cwdm wavelength grid*, 2019. [Online]. Available: https://www.itu.int/rec/T-REC-G.694.2.

[28] ITU, *G.652 : Characteristics of a single-mode optical fibre and cable*, 2016. [Online]. Available: https://www.itu.int/rec/T-REC-G.652/.

[29] S. M. Kay, *Fundamentals of statistical signal processing: estimation theory*. Hoboken, NJ, USA: Prentice-Hall, 1993.

[30] F. Olofsson, M. Karlsson, T. Eriksson, and C. Fager, "Investigation of fiber length differences in distributed MIMO Sigma-Delta-over-Fiber systems," in *49th European Conf. on Opt. Commun.*, Oct. 2023, pp. 968–971.

[31] A. Goldsmith, *Wireless Communications*. Cambridge, United Kingdom: Cambridge Univ. Press, 2005.

[32] 3GPP, *NR Base Station (BS) radio transmission and reception*, TS 38.104 version 18.6.0 Rel. 18, 2024.

[33] I. C. Sezgin, T. Eriksson, J. Gustavsson, and C. Fager, "A Flexible Multi-Gbps Transmitter Using Ultra-High Speed Sigma-Delta-over-Fiber," in *IEEE MTT-S Int. Microw. Symp. Dig.*, Jun. 2018, pp. 1195–1198.

[34] S. B. Weinstein, "The history of orthogonal frequency-division multiplexing," *IEEE Commun. Mag.*, vol. 47, no. 11, pp. 26–35, Nov. 2009.

[35] E. Dahlman, S. Parkvall, and J. Sköld, *5G NR : the Next Generation Wireless Access Technology*. San Diego, CA, USA: Elsevier Science & Technology, 2018.